Equation-of-State Measurements of Porous Materials on OMEGA: Numerical Modeling

Introduction

The equation of state (EOS) of materials at high densities and pressures is of wide interest to inertial confinement fusion (ICF), planetary physics, and astrophysics. The EOS at these conditions often involves a mixture of atomic, ionic, and molecular species, making *ab initio* theoretical modeling prohibitive. Experiments to constrain EOS models have been performed using static methods such as diamond-anvil cells[1] and at higher pressures using dynamic methods, such as shocks generated by light-gas guns,[2] lasers,[3] and even nuclear explosions.[4,5] Of these methods, laser-driven shocks currently provide the best method available for not only accessing the high pressures of interest, but performing accurate measurements necessary to determine the EOS.

The Hugoniot of a material is the set of thermodynamic states, e.g., pressure and density, that can be reached after the propagation of shock waves of various strengths through the material. The measurement of a Hugoniot represents only a finite number of points along a single line through pressure–density space. While this by no means uniquely determines the EOS, it may constrain it. If the experimental data are determined to a great enough precision, they may even (as is hoped for in the impedance-matching measurements of deuterium) rule out competing EOS models.[6] Even though Hugoniot data may not constrain all regions of the EOS, the principal and secondary Hugoniots are of primary interest in applications relevant to ICF, since the gain of target designs is sensitive to the timing of two shocks for most direct-drive designs and as many as four shocks for indirect-drive designs.

Foams play a key role in the so-called above-ground experiments of the Stockpile Stewardship Program (SSP).[7] In support of the SSP, a series of experiments designed to study the EOS of foams began in the past year at LLE. In addition, high-gain, direct-drive ICF target designs have been proposed that use foams, making their properties of interest in ICF as well. For instance, in the designs of Colombant *et al.*,[8] foam is used as ablator material, in conjunction with an outer layer of a high-atomic-number material such as Au. In these designs, the foam is preheated by radiation from the outer layer and has substantially higher ablation velocities, resulting in a more stable outer surface. In other "wetted-foam" designs,[9] the higher atomic number of the foam results in greater absorption and increased laser energy coupled into the target, allowing more fuel to be used, producing higher gain. The models of both Colombant[8] and Skupsky[9] use foam to increase the target performance, in contrast to earlier foam designs, which proposed the use of foam only as a matrix to contain liquid DT or as a means to reduce imprint.[10,11] Direct-drive ICF target designs usually use a pulse that drives two main shocks into the target. The performance of these targets depends in part on the timing of these shocks, making determination of the wetted-foam EOS essential.

Several laser-driven shock experiments have been performed to determine the Hugoniot of foams of various densities and constituent materials. Benuzzi *et al.*[12] and Batani *et al.*[13] determined the shock speed and post-shock pressure as a function of initial foam average density for values from 5 to over 1000 mg/cc, for TMPT [trimethylol propane triacrylate $(C_{15}H_{20}O_6)$]. Koenig *et al.*[14] subsequently determined the pressure as a function of density for a range of initial TMPT foam densities, comparing their results to a Hugoniot calculated with the *SESAME* EOS, and inferring the amount of preheat necessary for agreement. The experiments performed at LLE complement these by focusing on carbonized resorcinol aerogel foam (CRF), a carbonized derivative of resorcinol formadlehyde (RF).[15] Aerogels are generally of interest because of their ultrafine cell and pore sizes (smaller than 1000 Å; by comparison, TMPT has pore sizes ~1 μm). Also, the carbonized derivative CRF has the benefit of greater material strength. CRF is being studied specifically because of its use in the Stockpile Stewardship Program. Unlike RF, CRF is optically opaque, potentially complicating the characterization that is necessary for application in ICF wetted-foam targets. For this reason, RF, TMPT, CH, and other foams similar to TMPT (such as divinyl benzene and ethyleneglycol dimethacrylate) are of potential interest for ICF target designs.

Because of their porosity, shocked foams exhibit behaviors not found in continuous materials: For example, if the porosity is large enough, it is possible for the shocked foam to have a lower density than that of its composite material. Probing the properties of shocked foams provides the potential for greater understanding of the structural physics of porous materials.

This article describes ongoing efforts at LLE to investigate the properties of CRF at high pressures and densities, focusing on the theoretical design of the experiments. In the following section the method used to determine the Hugoniot of foam samples is described as well as the resulting sensitivity to experimental uncertainty. Following that, the procedure used to calculate the Hugoniot is presented. The simulations used to design the experiments are then described, as well as the requirements placed on the target and pulse for a high-accuracy Hugoniot measurement experiment. These are followed by a discussion of the results.

The Impedance-Matching Method

When a sound wave encounters an interface between two materials, the strength and properties of the reflected and transmitted waves are determined by the *acoustic impedance* ρc, where ρ is the density and c the sound speed, in the two materials: if the acoustic impedance is continuous across the interface, the wave travels from one material to the other without changing speed; otherwise a wave is reflected as well as transmitted. As a sound wave is essentially a weak shock wave traveling at the sound speed, the behavior for a strong shock is similar: The acoustic impedance is replaced by the product of the density with the shock speed, ρU_s. If the shock encounters an increase in this quantity at a material interface between two materials, a shock is reflected back into the first material as well as transmitted into the second; otherwise a shock is transmitted and a rarefaction wave reflected. (A rarefaction wave is a propagating region that grows in time, in which the density and pressure drop as the material is accelerated.)

The *impedance-matching method*[16] uses the interaction of a shock wave with an interface between materials of different "hardness" (ρU_s) to determine a material's Hugoniot using the EOS of a reference material. A shock is sent through a layer of material of known EOS into a layer of the material under study (e.g., foam) in contact with the known material. Al is used as a reference material since it has been well characterized in previous studies at the pressures of interest here.[17] In these experiments the shock is generated by laser-driven ablation. The Rankine–Hugoniot (RH) jump equations for pressure and

density provide two equations for the post-shock conditions (pressure p and density ρ) in the foam in terms of the known initial conditions (pressure p_0 and density ρ_0), the shock speed U_s, and the post-shock particle speed U_p. These conditions are applied across the shock front in both the Al and the foam, giving four equations in eight unknowns. Assuming that no gap forms between the Al and the foam, the pressure and the post-shock speed are continuous across that interface, providing an additional two constraints. Thus, measurement of the shock speeds in the two materials is sufficient to fully describe the system. (The shock speed is assumed to be equal to the average shock speed.) Measurement of the shock-breakout times from the Al and foam using the VISAR interferometer[18] allows determination of the average shock speed in each layer. The particle speed in the foam is inferred from the measured average shock speed in the Al, combined with knowledge of the Al EOS. This process is described in detail in the next section.

The reason the impedance-matching method was chosen for these experiments can be seen by examination of alternate methods. Other methods that have been used to determine a material's Hugoniot include the following: (1) The symmetric method, involving colliding two planar samples, where both the sample speed before contact and the resulting shock speed are measured. This method has the advantage of not relying upon knowledge of the EOS of a standard material. It requires, however, that the material speed be measured, for instance with side-on radiography. It also requires that the sample withstand being driven by the laser without bowing or loss of structural integrity. (2) The reshock method, which is similar to the impedance-matching method, except that the shock is sent first through the unknown sample, and subsequently into the material of known EOS. As in impedance matching, measurement of the shock speeds in both materials allows determination of the shocked state of the material of unknown EOS, given knowledge of the EOS of the standard. Because the former is shocked twice, this method allows access to higher pressures than the impedance-matching method. Computation of the Hugoniot, however, is less accurate. (3) A modification of the impedance-matching method has been suggested[19] in which a foot pulse is used to raise the entire target to a higher initial pressure (given by the ablation pressure) after which the intensity is increased and a main shock is launched and tracked using side-on x-ray radiography. This method allows access to still higher pressures but also requires that the laser pulse be sufficiently long for pressure equilibrium to be reached, which may be prohibitively long. (These methods and other methods

for experimentally ascertaining EOS properties without determining the Hugoniot are discussed in Refs. 16 and 20.)

In addition to the standard impedance-matching method, the experiments on OMEGA will explore the *direct* method, in which both the shock speed and the (post-shock) particle speed are measured using side-on radiography (e.g., see Ref. 21). This method replaces the error introduced by using a known EOS to determine the particle speed with the uncertainty, which may be lower, of determining the interface position from side-on radiography.

Calculation of the Hugoniot and Sensitivity to Measurement Uncertainty

As mentioned above, the Hugoniot of the foam is calculated using the known Hugoniot and isentrope of the reference material. For the data shown here, a quotidian-equation-of-state (QEOS)[22] table for Al was used.[23] In principle, any reference EOS may be used to determine the conditions (pressure, density, fluid speed) in the foam after the passage of the primary shock. When the primary shock enters the foam from the Al (which has a higher acoustic impedance), a rarefaction wave (RW) is sent back into the Al. This RW has the effect of equalizing the pressure and velocity in the Al and foam. This is shown schematically in Fig. 90.6, which contain plots of the pressure and density near the Al/foam interface (the dashed line in Fig. 90.6) before [(a) and (b)] and after [(c) and (d)] the shock has passed from the Al into the foam. Assuming there are no gaps between the Al and the foam, the velocity and pressure on either side of the interface (that is, regions *i* and *ii*) must be equal. Thus, the post-shock pressure and velocity in the foam are equal to the values in the Al after the passage of the RW. In Fig. 90.6(c) and 90.6(d) this is shown by the continuity of the pressure across the interface. Since the EOS of the Al is known, these conditions (in region *ii*) may be used to determine the conditions in the Al before the RW, but after the passage of the primary shock (i.e., region *iii*).

This process is shown graphically in Fig. 90.7. The RH jump conditions for mass, pressure, and energy are given by, respectively,

$$\rho\left(U_s - U_p\right) = \rho_0\left(U_s - U_0\right),$$

$$p - p_0 = \rho_0\left(U_s - U_0\right)\left(U_p - U_0\right),$$

$$E - E_0 = \frac{1}{2}\left(p + p_0\right)\left(V_0 - V\right),$$

where ρ is the density, p is the pressure, E is the internal energy, $V = 1/\rho$, zero subscripts refer to pre-shock values, U_s is the shock speed, and U_p is the post-shock speed.[16] The Al standard EOS is used in a form tabulated by isotherms. The states that lie on the Hugoniot may be determined for a given isotherm using the RH equation for energy. For the strong shocks considered here, the initial pressure and energy are much smaller than their post-shock values and may be taken to be zero. Combining the RH equations for mass and momentum, and setting $U_0 \rightarrow 0$ (as is the case in the experiment), the shock speed is given along the Hugoniot by

$$U_s^2 = \frac{p - p_0}{\rho - \rho_0} \times \frac{\rho}{\rho_0}.$$

The point along the Hugoniot (the solid line in Fig. 90.7) corresponding to the state of the Al just after the passage of the primary shock is that for which U_s is given by the measured shock speed U_{Al}.
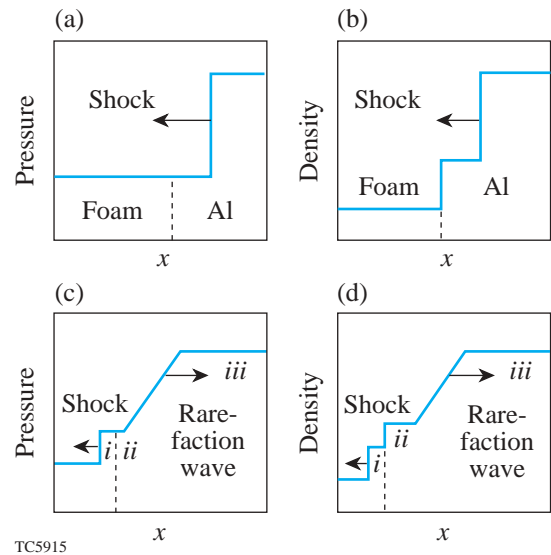

Figure 90.6
A schematic representation of the pressure and density near the Al/foam interface (represented by a dashed line) before [(a) and (b)] and after [(c) and (d)] passage of the shock from the foam into the Al. When the shock passes into the foam, a rarefaction wave is sent back into the Al, equalizing the pressure and velocity in the two materials. Notice that while the density changes across the interface, the pressure is continuous.

Assuming radiative losses are insignificant, the RH equations are satisfied, and the states reached by the RW lie along the release isentrope (the dashed line in Fig. 90.7) intersecting the shocked Al state determined above. The release isentrope may be calculated simply by finding, for each isotherm, the states for which the entropy is unchanged. The entropy change is given in terms of temperature and density changes by

$$ds = c_v \frac{dT}{T} - \left. \frac{dp}{dT} \right|_\rho \frac{d\rho}{\rho^2}$$

(see, e.g., Ref. 24). The particle speed along the release isentrope is computed using the relation (see, e.g., Ref. 20)

$$U_p = \int_{\rho_0}^{\rho} c_s(\rho) \, d\ln\rho = -\int_{V_0}^{V} \left(-\frac{\partial p}{\partial V} \right)_s^{1/2} dV.$$

The final state along the isentrope reached by the RW is that intersected by the Rayleigh line given by the RH momentum equation in the foam (again, where $U_0 = 0$), $p = \rho_0 U_{\mathrm{foam}} U_p$.

Finally, once the post-shock pressure and particle speed in the foam are calculated, the post-shock foam density may be found from the RH mass equation

$$\rho_{\mathrm{foam}} = \rho_0 U_{\mathrm{foam}} / \left(U_{\mathrm{foam}} - U_p \right).$$

Uncertainty in the calculated Hugoniot is due to both the uncertainty in the measurement of the shock speeds and the calculation of the post-shock pressure and density in the foam. The final uncertainty δP in the pressure, for instance, given the measured uncertainties δU_{Al} and δU_{foam} in the shock speeds, is given by

$$\delta P = \sqrt{ \left(\frac{\partial P}{\partial U_{\mathrm{Al}}} \delta U_{\mathrm{Al}} \right)^2 + \left(\frac{\partial P}{\partial U_{\mathrm{foam}}} \delta U_{\mathrm{foam}} \right)^2 },$$

and likewise for the uncertainty δU_p in the foam post-shock particle speed. The necessary partial derivatives are calculated numerically by calculating $\Delta P(\Delta U_{\mathrm{Al}}, \Delta U_{\mathrm{foam}})$, in the limit that $\Delta U_{\mathrm{Al}} \to 0$ or $\Delta U_{\mathrm{foam}} \to 0$. The values of the calculated partial derivatives are required to converge in these limits in order to calculate the final uncertainty. The uncertainty $\delta\rho$ in the density is given by the chain rule:

$$\delta\rho_{\mathrm{foam}} = \frac{\partial \rho_{\mathrm{foam}}}{\partial U_p} \delta U_p = \frac{\rho_0 U_{\mathrm{foam}}}{\left(U_{\mathrm{foam}} - U_p \right)^2} \delta U_p.$$

As can be seen from this expression, the closer the shock speed is to the particle speed in the foam, the more uncertain the determination of the foam post-shock density. For example, consider an experiment with shock speeds of 28 μm/ns in the Al and 40 μm/ns in the foam. The corresponding post-shock
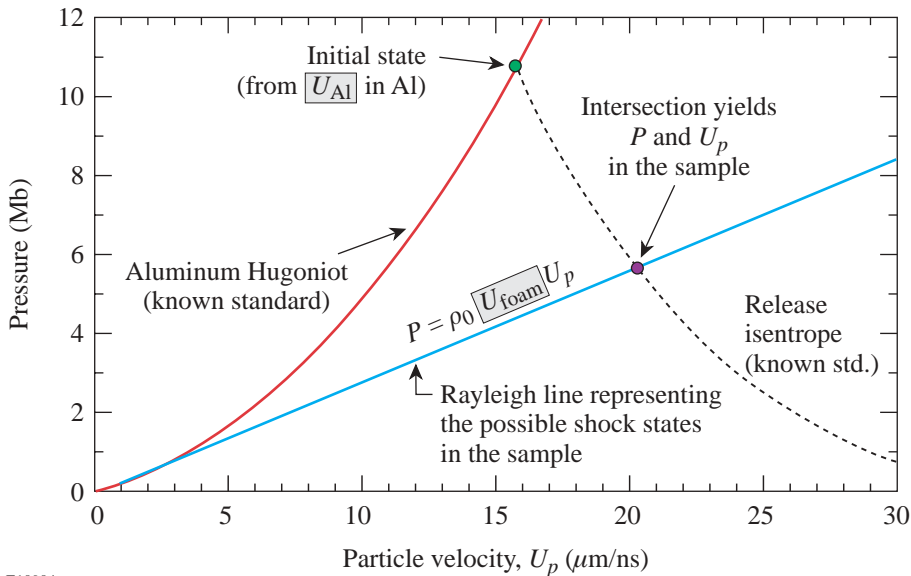

Figure 90.7
A graphical representation of the process used to determine the foam Hugoniot from the measured shock speeds.

E10904a

conditions in the foam are $\rho = 0.59$ g/cc and $p = 1.3$ Mbar. To achieve an uncertainty of even 0.1 g/cc (17%) in the calculated density, the measured uncertainty in the shock speeds (assuming they are equal) must be less than ~2%. The corresponding uncertainty in the pressure is ~13%.

The preceding procedure to determine the Hugoniot may be performed, for purposes of estimation, entirely analytically if a linear relationship is assumed between the shock and particle speeds in the Al, $U_{Al} \approx C + sU_p$ (see, e.g., Ref. 20). For the Al *SESAME* table[25] these constants are given approximately by $C \sim 5.35$ km/s, $s \sim 1.34$ for shock speeds between 10 and 30 km/s. In this case the uncertainties may also be estimated analytically.[26,27]

Target Design

As described above, only *average* shock speeds are measured experimentally. To accurately determine the Hugoniot, the target and pulse must be designed so that the shock is steady. The primary shock will remain steady in the Al and CRF only if it is not overtaken by secondary rarefaction waves and shocks generated by the passage of the primary shock between different material layers.

At least three other factors constrain the design of the target: First, the uncertainty in the measured average shock speed is less for a thicker layer, since it is based on a determination of the breakout time of the shock. Second, at the end of the laser pulse a rarefaction wave (RW) is sent into the target. It can be shown[28] that the RW always moves faster than the primary shock because the post-shock fluid speed plus the sound speed in the post-shock material is greater than the shock speed. The duration of the pulse must be sufficient so that the RW does not reach the primary shock before it breaks out of the target. (For a single-layer target, the RW catches the primary shock at about a time equal to twice the pulse duration.[29]) Third, the ablator layer(s) must be of a sufficient optical thickness to prevent radiation from the corona from preheating the sample layers. Preheat not only changes the initial conditions seen by the shock but nonuniformly alters the temperature and density, affecting shock steadiness. The effects of radiative preheat are discussed further in the next section. (For a further discussion of preheat effects see Ref. 30.)

Figure 90.8 shows a space–time diagram from a *LILAC* simulation[31] of a sample target. (All *LILAC* simulations described here use the *SESAME* EOS.[32]) A schematic of the target is shown in Fig. 90.9. The 1-D simulation represents a slice parallel to the *x* axis, which cuts through the thin side of

the Al step and the foam. The locations of the shocks and RW's in Fig. 90.8 are determined from the local variations in inverse pressure scale length $|L^{-1}| \equiv |\partial \ln p / \partial x|$ (in μm^{-1}), where p is the pressure and x is the distance into the target. For clarity in identification of shocks and RW's, the target in this simulation is driven by a steady 3.5-ns, 200-TW/cm^2 laser pulse. The RW launched from the ablation surface at the end of the laser pulse may be seen in the neighborhood of 3.6 ns, 100 μm. Note that the reflected RW from the Al/CRF interface results in a second, inward-traveling shock when it reaches the ablation surface.

To predict shock steadiness and compare the results of simulations with experimentally measured shock speeds, the shock position and velocity must be determined from *LILAC* simulations. The former is found by determining the location of the local maxima of L^{-1}. These correspond to abrupt changes in the pressure, due to both shocks and material interfaces. Some of these maxima may be ruled out by requiring that $L > 0$. Two additional criteria aid in locating the shock: First, since the global maximum of L^{-1} is often the rear surface (farthest from the laser) of the foam, the local maximum closest to the front (or laser side), in most targets, corresponds to the shock. Second, the shock may also be identified as the maximum nearest to a local maximum in the derivative dT_e/dt of the electron temperature T_e with respect to time t, allowing the shock position to be unambiguously identified numerically.

Once the cell containing the position of the shock is determined as a function of time, the shock speed is computed: the location of the shock within a cell is approximated by fitting a parabola to $L^{-1}(x)$, using the value of L^{-1} in the cell, combined with $\partial L^{-1}/\partial x$ in the two neighboring cells. Due to the finite time resolution of the simulation, the shock velocity determined by differentiating the shock position is noisy. The noise has a time scale comparable to $\Delta z/U_s$ and, by choosing grid spacing Δz, can be made much smaller than the time scale for physical changes in U_s (due to, for instance, secondary shocks and rarefaction waves, and temperature and density gradients due to preheat). This noise is then removed by performing a linear regression at each time using n previous and subsequent values of the velocity. This least-squares fit acts as a low-pass filter, removing fluctuations in the shock speed having frequencies higher than $f \sim (2n\Delta t)^{-1}$, where Δt is the time interval for simulation output. (Note that Δt is typically much larger than the simulation time step.) As a result, the time interval for simulation output must be chosen to ensure that no hydrodynamic behavior of interest is removed during the smoothing process. A plot of the shock speed versus time for a typical target is shown in Fig. 90.10.
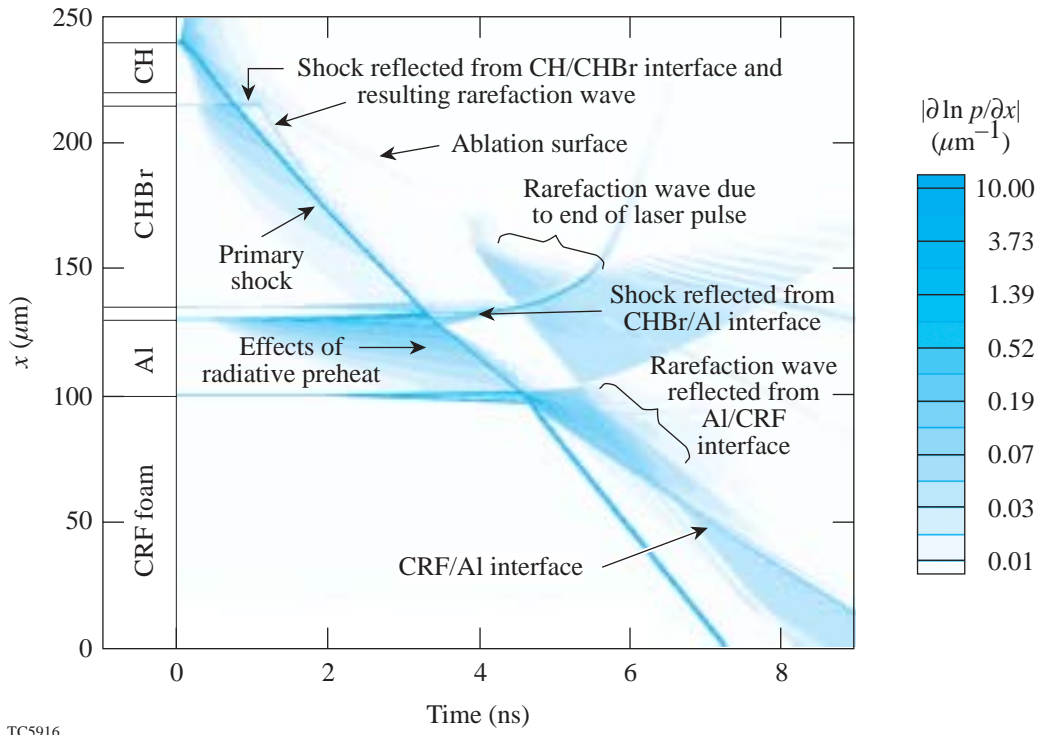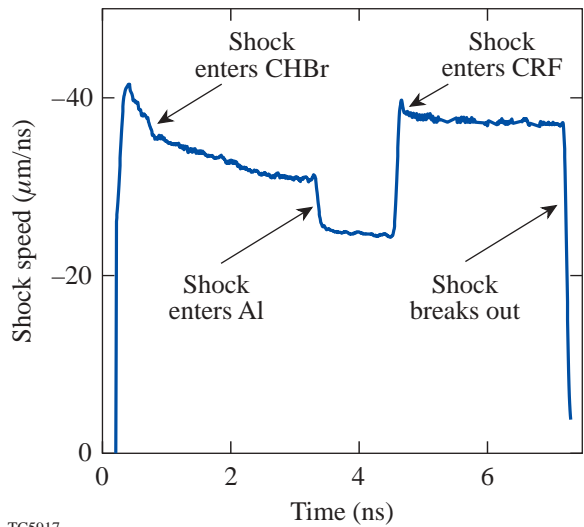
TC5916

Figure 90.8
A space–time diagram from a *LILAC* simulation of a standard target. The location of the shocks and rarefaction waves (RW's) are determined from the local variations in inverse pressure scale length $\left|\partial \ln p / \partial x\right|$ (in μm^{-1}), where p is the pressure and x is the distance into the target. Note the RW's and secondary shocks that are generated when the primary shock reaches each material interface.
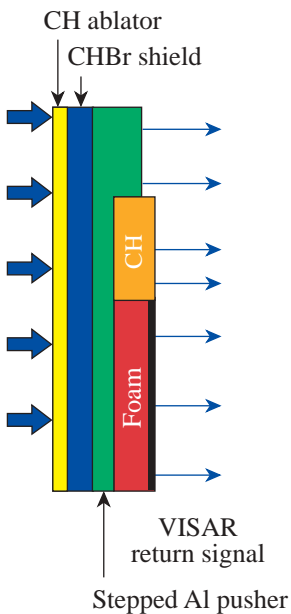
Shot 23860
E11040b

Figure 90.9
The structure of a standard target used in the EOS experiments on OMEGA. The target consists of a CH ablator, a CHBr radiation shield, a stepped Al layer, and a foam layer. Some of the targets also have a "witness plate" of, for instance, plastic, which is transparent to the VISAR laser.

TC5917

Figure 90.10
The primary shock speed as calculated from the *LILAC* simulation corresponding to Fig. 90.6. The rapid drop in the calculated shock speed at 7.2 ns corresponds to the breakout of the shock from the CRF. In this and other shock plots in this article, oscillations with periods of tens of picoseconds are due to numerical noise.

The targets used in these experiments initially consisted of a 20-μm-thick CH ablator, a 30-μm-thick Al layer (and 100 μm on the thick side of the Al step), and a 100-μm-thick foam layer. The resulting shock speed was found to be less steady than desired. Following Glendinning *et al.*,[33] an 80-μm-thick brominated-plastic layer was added after the CH ablator to serve as a radiation shield to prevent preheat. Radiative preheat causes a continuous change in the pre-shock temperature, density, and pressure. The speed of the primary shock changes as a result of the varying pre-shock conditions. In Fig. 90.11 a comparison of the computed shock speeds shows the improved shock steadiness when the CHBr radiation preheat shield is used. The steadiness of the shock may be measured by the standard deviation of the shock speed. (The steadiness σ is then given by a time-weighted average of the steadiness in the Al and the foam.) Without the CHBr preheat shield, $\sigma \sim 1.75$ μm/ns, and with the shield, $\sigma \sim 0.37$ μm/ns.

for higher shock pressures. This behavior occurs because, for strong shocks in this regime, the thermal pressures produced in crushing the foam can become very large, resulting in lower densities. Note that while the final density ρ is lower than that of the constituent ($\rho_c \sim 1$ g/cc for a CH foam, for instance), it is still higher than the average initial foam density ρ_f, so that $\rho_f < \rho < \rho_c$. This anomalous behavior is described in Ref. 16 and has been observed in other materials as well.[5] This anomalous behavior is not seen in the 0.4-eV and 1-eV curves, indicating that at small preheat values the foam begins to behave more like a continuous solid. Impedance-matching experiments by Koening *et al.*[14] also found that agreement between the experimental and theoretical EOS's could be obtained only by assuming a small amount of preheat.

Figure 90.12
The Hugoniot calculated from the QEOS, for a room-temperature CRF foam (solid), a 0.4-eV foam (dashed), and a 1-eV foam (dashed–dotted). Notice that the Hugoniots for the heated foams do not show the anomalous behavior of decreasing density with increasing pressure.
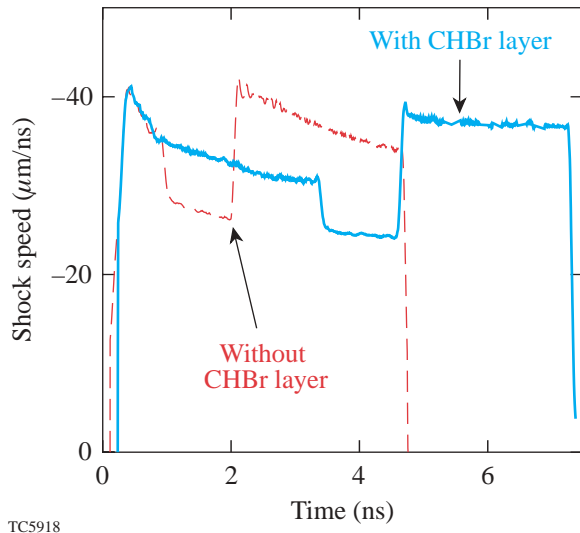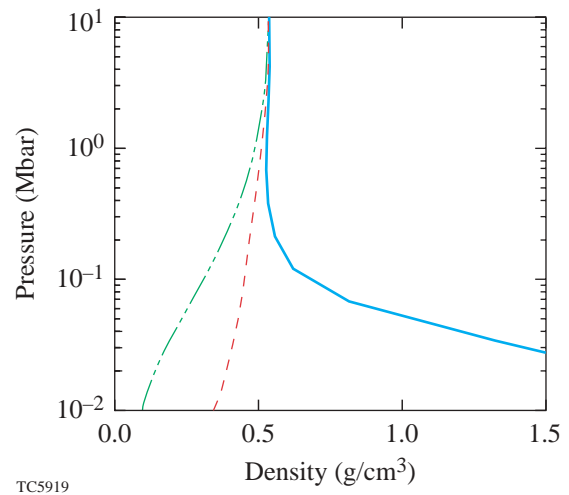

Figure 90.11
The shock speed for targets with (solid) and without (dashed) an 80-μm CHBr preheat shield, showing its effectiveness at reducing radiative preheat and the resulting increase in shock steadiness.

In addition to affecting shock steadiness, even a small amount of preheat may alter the Hugoniot for moderate and low pressures. Figure 90.12 shows the Hugoniot for CRF as calculated from QEOS, assuming 0.0252-eV (room temperature), 0.4-eV, and 1-eV initial temperatures. The room-temperature curve show a well-documented feature of porous materials, namely a Hugoniot that curves to lower densities

Because the ablation pressure scales with the laser intensity as $p \propto I^\alpha$, where $\alpha \approx 2/3$ (Ref. 34) and because the pressure is proportional to the square of the shock speed for strong shocks, a temporal intensity perturbation would be expected to result in a shock speed perturbation of $\delta U/U_0 \approx (1/3)\delta I/I_0$. However, the laser drive is coupled to the post-shock target material through the conduction zone. As a result, the system behaves like a driven, damped harmonic oscillator, and perturbations in the drive of sufficiently high frequency have no significant effect on the primary shock. This may be seen in the shock speeds from simulations of a typical target in which 10%

amplitude modulations with 250-ps and 1-ns periods are imposed on a flattop pulse (see Fig. 90.13). (These pulses include a 100- to 200-ps rise and fall taken from a typical measured pulse.) These periods were chosen as characteristic of the time scales for variations observed in typical shots on OMEGA. The amplitude modulations launch a sequence of shocks (alternated with rarefaction waves) into the target, causing jumps in the shock speed when they catch up to the primary shock. For a 20-TW/cm^2 pulse, which produces a 440-kbar shock in the foam, the 1-ns modulation results in $\sigma \sim 3.7\%$, while the 0.25-ns modulation perturbs the shock speed in the foam by only $\sigma \sim 1\%$.
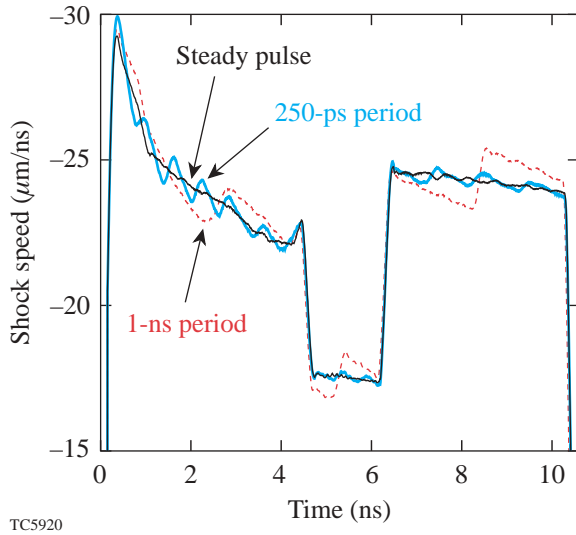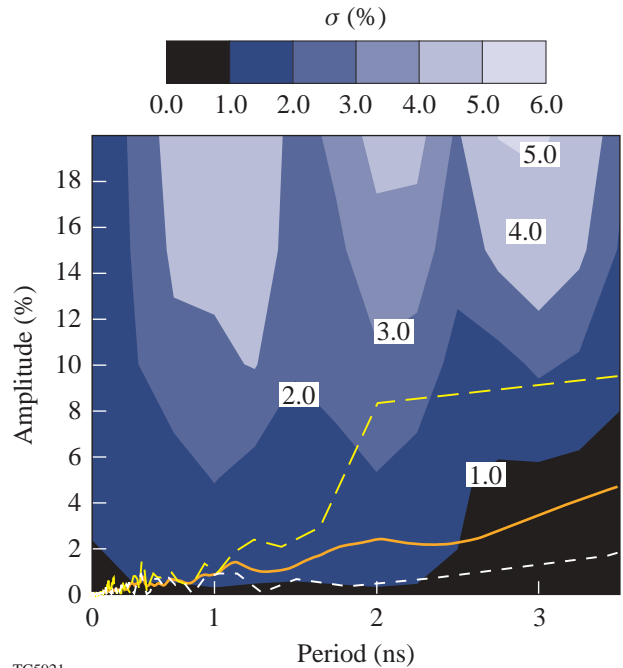

Figure 90.13

Shock speed for three simulations: one with a perfectly flat pulse (thick solid) and two with 10%-amplitude-modulated pulses with periods of 250 ps (thin solid) and 1 ns (dashed). All three pulses have a realistic 100- to 200-ps rise and fall taken from a typical measured pulse. Pressure modulations from the modulated pulse steepen into distinct shocks by the time they reach the primary shock, resulting in abrupt jumps in shock speed, as at 8 ns.

The σ for a range of perturbation periods and amplitudes is shown in Fig. 90.14. These data were computed using an array of *LILAC* simulations, with periods of 250 ps, 0.5 ns, …, 3.5 ns; amplitudes of 5% (1 TW/cm^2), 10%, 15%, 20%; and compared to a simulation with a flattop pulse.

Because the shock speed as a function of time in the Al and foam is not steady, it is possible (though unlikely) for a perturbed pulse to result in decreased standard deviation of the shock speed about the mean. For this reason, we have

also computed the standard deviation σ_f not about the mean, but with respect to the shock speed of a flattop pulse (see Fig. 90.15).

For comparison, the discrete Fourier transforms of 32 pulses, with a range of average intensities from 4 TW/cm^2 to almost 100 TW/cm^2, from two experimental campaigns performed on OMEGA in October and November 2001, were computed (see Fig. 90.16). The contour lines associated with an average spectrum (heavy solid curves) as well as a best and worst (dashed curves) (using linear interpolation for non-integral mode numbers) for this set of shots are shown in Figs. 90.14 and 90.15. These figures show that for a typical OMEGA pulse, the unsteadiness of the shock may be expected, from 1-D simulations, to be below 1.5%.

Figure 90.14

The standard deviation σ about the mean of the shock speed, during the shock transit through the Al and foam. The steadiness is shown as a fraction (in %) of the mean shock speed. For comparison, the average discrete Fourier transform of 32 shots from two EOS experiments is also shown (solid), as well as a best and worst spectrum (dashed). The sharpness of the contour lines reflects the finite number of simulations used. Note that because the period of the perturbations can be comparable to the hydrodynamic time scale, the phase of the perturbations can be important for larger amplitudes, creating the local extrema in σ [and in σ_f in Fig. 90.15 (see below)].
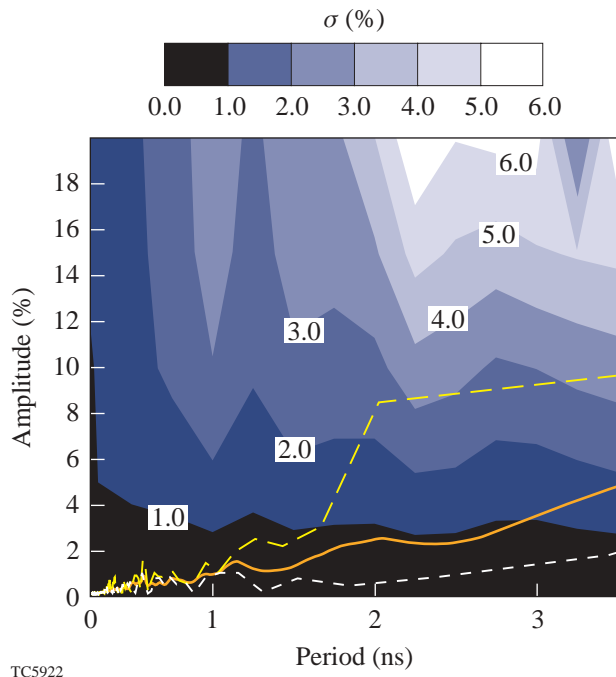
TC5922

Figure 90.15
The standard deviation, as in Fig. 90.14, but computed with respect to the shock speed for a steady pulse, rather than with respect to the mean.
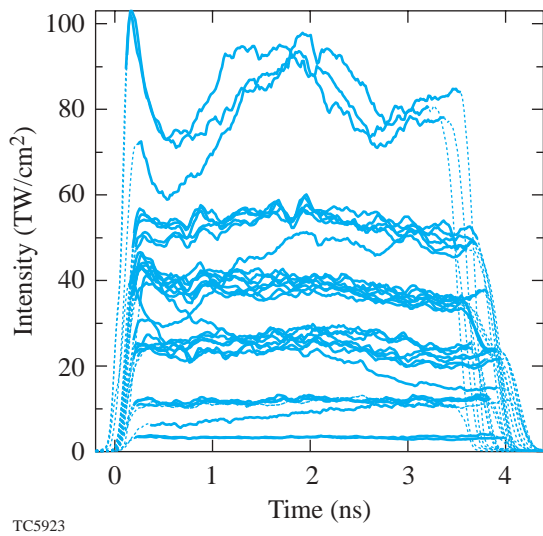

TC5923

Figure 90.16
The pulses used in the comparisons shown in Figs. 90.14 and 90.15. Before computing the Fourier transforms, the rise and fall of the pulses were removed (dotted).

The preceding conclusion is based on the assumption that, since the amplitudes of the modulations are small, the modes remain linear. An additional simulation that was performed using an average pulse shape (of the normalized measured pulses) resulted in a pulse unsteadiness σ of 1.44%, to be compared to the 0.95% of the perfectly flattop pulse. This supports the conclusion that the typical pulse steadiness on OMEGA will in general, for this intensity, result in shock steadiness of less than ~1.5%.

Due to 2-D effects, such as shock curvature and transverse radiative transport,[35] defocusing of the beam by the corona,[33] and lateral plasma flow,[36] 1-D simulations systematically overestimate the shock speed. Fortunately, determining the foam Hugoniot requires only the EOS of Al, along with the measured shock speeds, and does not depend on precise agreement between the simulated and measured shock-breakout times. A comparison of experimental results with 1-D simulated shock speeds, in which the intensity was reduced to account for 2-D effects, is shown in Fig. 90.17. For this shot (27174) a 20% reduction was needed. In general, a sufficient margin is built into the 1-D target designs to allow for the systematic decrease in shock speed due to 2-D effects.
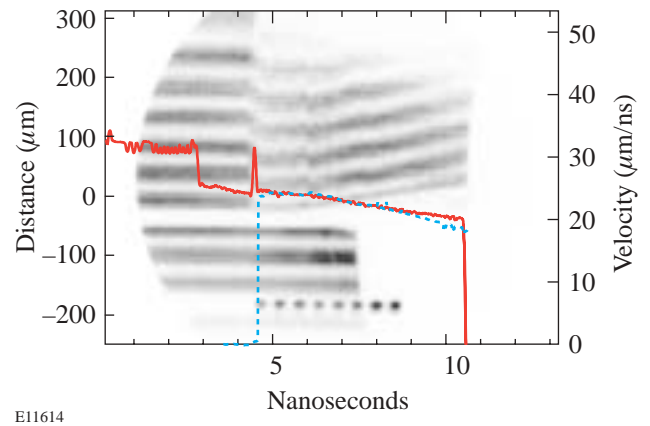

E11614

Figure 90.17
A comparison of the measured (dashed) and simulated (solid) shock speeds for shot 27174. To model 2-D effects, the intensity of the measured pulse was uniformly decreased by 20%. This target consisted of 20 μm CH, 5 μm glue (modeled by CH), 80 μm CHBr, 5 μm glue, 40 μm Al, and 140 μm quartz. The transparent quartz layer was used to determine shock speed as a function of time, for comparison with simulation. Because the density of quartz is close to that of Al, it also provides an indication of the typical shock speeds in the thick portion of the Al step. The measured shock speed was determined from the motion of the ASBO/VISAR fringes, which are also shown. The simulation and experiment were synchronized to the time of shock breakout into the quartz.

Discussion and Conclusions

A description of the theoretical tools used in the design of targets has been presented here, including the constraints presented by the requirement of minimal radiation preheat and shock steadiness. Even a small amount (0.4 eV) of preheat can alter the Hugoniot at pressures of less than 1 Mbar for 100-mg/cc CRF foam, potentially constraining the amount of allowable preheat. It has also been shown that the pulse steadiness of typical pulses on OMEGA is sufficient to ensure, on average, shock steadiness of less than 1.5% (for a typical 20-TW/cm^2, 3.5-ns pulse). If the measured shock speeds have an error of 1.5%, the resulting uncertainty in the density and pressure will be ~6.6% and ~2.4%, respectively, for a shock generated by laser illumination of this intensity. While this result does not rule out the effects of pulse steadiness, it suggests that other aspects of the experiment should be improved as well. Future experiments will also focus on the use of the "direct method," in order to reduce the uncertainty in the computed density by providing a direct measure of target compression.

REFERENCES

1. R. J. Hemley and H. K. Mao, Phys. Rev. Lett. **61**, 857 (1988).

2. A. H. Jones, W. M. Isbell, and C. J. Maiden, J. Appl. Phys. **37**, 3493 (1966).

3. C. G. M. van Kessel and R. Sigel, Phys. Rev. Lett. **33**, 1020 (1974).

4. L. V. Al'tshuler *et al.*, Sov. Phys.-JETP **34**, 606 (1958).

5. R. F. Trunin, *Shock Compression of Condensed Materials* (Cambridge University Press, Cambridge, England, 1998).

6. G. W. Collins *et al.*, Science **281**, 1178 (1998).

7. R. Jeanloz, Phys. Today **53**, 44 (2000); *High-Energy-Density Physics Study Report*, National Nuclear Security Administration, U.S. Department of Energy, Washington, DC (6 April 2001).

8. D. G. Colombant *et al.*, Phys. Plasmas **7**, 2046 (2000).

9. S. Skupsky, R. Betti, T. J. B. Collins, V. N. Goncharov, D. R. Harding, R. L. McCrory, P. W. McKenty, D. D. Meyerhofer, and R. P. J. Town, "High-Gain, Direct-Drive Target Designs for the National Ignition Facility," to be published in the *Proceedings of the 2nd International Conference on Inertial Fusion Sciences and Applications*.

10. L. M. Hair *et al.*, J. Vac. Sci. Technol. A **6**, 2559 (1988).

11. M. Desselberger *et al.*, Phys. Rev. Lett. **74**, 2961 (1995).

12. A. Benuzzi *et al.*, Phys. Plasmas **5**, 2827 (1998).

13. D. Batani *et al.*, Plasma Phys. Control. Fusion **40**, 1567 (1998).

14. M. Koenig *et al.*, Phys. Plasmas **6**, 3296 (1999).

15. R. W. Pekala and F-M. Kong, Lawrence Livermore National Laboratory, Livermore, CA, UCRL-99846 (1988).

16. Ya. B. Zel'dovich and Yu. P. Raizer, in *Physics of Shock Waves and High-Temperature Hydrodynamic Phenomena*, edited by W. D. Hayes and R. F. Probstein (Academic Press, New York, 1966).

17. J. H. Campbell *et al.*, Laser Part. Beams **15**, 607 (1997).

18. L. M. Barker and R. E. Hollenbach, J. Appl. Phys. **43**, 4669 (1972).

19. J. W. Bates and A. N. Mostovych, Bull. Am. Phys. Soc. **46**, 43 (2001).

20. G. R. Gathers, *Selected Topics in Shock Wave Physics and Equation of State Modeling* (World Scientific, Singapore, 1994).

21. R. Cauble *et al.*, Phys. Plasmas **4**, 1857 (1997).

22. R. M. More *et al.*, Phys. Fluids **31**, 3059 (1988).

23. D. A. Young, Lawrence Livermore National Laboratory, private communication (2001).

24. F. Reif, *Fundamentals of Statistical and Thermal Physics* (McGraw-Hill, New York, 1965).

25. S. P. Marsh, ed. *LASL Shock Hugoniot Data*, Los Alamos Series on Dynamic Material Properties (University of California Press, Berkeley, CA, 1980).

26. N. C. Holmes, Rev. Sci. Instrum. **62**, 1990 (1991).

27. A. C. Mitchell and W. J. Nellis, J. Appl. Phys. **52**, 3363 (1981).

28. R. Courant and K. O. Friedrichs, *Supersonic Flow and Shock Waves*, Pure and Applied Mathematics, v. 1 (Interscience, New York, 1948), p. 141.

29. R. J. Trainor and Y. T. Lee, Phys. Fluids **25**, 1898 (1982).

30. J. J. Honrubia *et al.*, J. Quant. Spectrosc. Radiat. Transf. **61**, 647 (1999).

31. M. C. Richardson, P. W. McKenty, F. J. Marshall, C. P. Verdon, J. M. Soures, R. L. McCrory, O. Barnouin, R. S. Craxton, J. Delettrez, R. L. Hutchison, P. A. Jaanimagi, R. Keck, T. Kessler, H. Kim, S. A. Letzring, D. M. Roback, W. Seka, S. Skupsky, B. Yaakobi, S. M. Lane, and S. Prussin, in *Laser Interaction and Related Plasma Phenomena*, edited by H. Hora and G. H. Miley (Plenum Publishing, New York, 1986), Vol. 7, pp. 421–448.

32. S. P. Lyon and J. D. Johnson, Los Alamos National Laboratory, Los Alamos, CA, Report LA-UR-92-3407 (1992).

33. S. G. Glendinning, D. K. Bradley, R. C. Cauble, M. J. Edwards, H. Louis, J. C. Moreno, S. J. Moon, B. A. Remington, E. J. Turano, T. R. Boehly, R. S. Craxton, and R. Town, Bull. Am. Phys. Soc. **45**, 199 (2000).

34. R. E. Kidder, Nucl. Fusion **8**, 3 (1968).

35. D. Braun *et al.*, Bull. Am. Phys. Soc. **46**, 44 (2001).

36. M. Temporal *et al.*, Il Nuovo Cimento **19D**, 1839 (1997).